Plasmonics
https://doi.org/10.1007/s11468-024-02293-6

RESEARCH

Dynamic Tunable Liquid-Core Photonic Crystal Fiber Sensor Based on Graphene Plasmon

Wei Luo[1] · Syeda Aimen Abbasi[1] · Xuejin Li[2] · Ho-Pui Ho[1] · Wu Yuan[1]

Received: 13 February 2024 / Accepted: 5 April 2024

Abstract

The combination of photonic crystal fiber (PCF) and graphene-supporting surface plasmon polaritons (SPP) presents a new approach to achieving a plasmonic sensor with adjustable properties in the terahertz (THz) frequency range. In this study, we investigate a liquid-core PCF-based graphene plasmonic sensor, where the analyte to be detected is located on both the sensing layer surface and the fiber core. As a result, the dispersion relations of both graphene plasmon (GP) and core-guide mode can be influenced by the analyte, leading to a negative refractive index (RI) wavelength sensitivity. This unique performance is attributed to the higher modulation degree of the core mode on the analyte RI (Δneff.core) compared to that of the GP mode (Δneff.GP). By reducing the graphene Fermi energy, a positive sensibility is achieved with the modulation relationship of Δneff.core < Δneff.GP. Subsequently, the geometry dependence is explored to optimize the sensing capabilities. Furthermore, we demonstrate the sensor's tunability by dynamically varying the graphene Fermi energy (E_f). By adjusting the E_f from 0.6 to 0.9 eV, the detection range can be artificially shifted from 0.554–0.574 THz to 0.686–0.724 THz, obtaining a tunability of 0.44 THz/eV and a higher sensitivity of 1.2667 THz/RIU. This design facilitates the efficient utilization of the limited bandwidth to detect various RIs and provides a flexible approach to constructing multiple sensing channels. To the best of our knowledge, this is the first report of graphene plasmonic sensing based on core-filled PCF in the THz frequency range. The novel analysis method of modulation degree and dispersion matching has the potential to be widely applied in THz plasmonic sensing and could lead to various nanoscience applications.

Keywords Graphene surface plasmon · Dynamic tunability · Photonic crystal fiber · Phase coupling

Introduction

The terahertz (THz) wavelength, covering a broad frequency range from 0.1 to 10 THz, is utilized in various applications such as biotechnology, telecommunication, imaging, and biomedical sensing [1–3]. Recent advancements in THz sources and detectors demonstrated various THz modulators based on metamaterials. Metamaterials, as artificially engineered and consisting of optical meta-atoms, are subwavelength resonators with highly confined and enhanced electrical fields that can manipulate light in unconventional ways [4, 5]. However, the modulators reported are limited to operating within a specific frequency range. In practical scenarios, it is essential to possess a robust adjustable operating frequency for dynamically modulating the performance without reconstructing the system. Graphene, a two-dimensional (2D) carbon-based material, has recently garnered significant attention due to its exceptional optoelectronic properties. One fascinating aspect of graphene is its capability to easily adjust carrier density through electrical control, enabling flexible alteration of performance with bias voltage rather than necessitating changes in the geometries [6–8]. Moreover, different from acting like an absorption material in the near-infrared range, graphene can support surface plasmon polaritons (SPP) in THz frequency like a metallic material. Therefore, graphene becomes a perfect candidate for designing a plasmonic modulator with dynamic tunability in the THz frequency [9–11].

Note that the free space electromagnetic waves cannot directly interact with the graphene plasmon (GP) due to the vector mismatch. Various approaches have been presented to enhance the light-graphene interaction. A typical way is

✉ Wu Yuan
wyuan@cuhk.edu.hk

[1] Department of Biomedical Engineering, The Chinese University of Hong Kong, Hong Kong 999077, China

[2] School of Science and Engineering, The Chinese University of Hong Kong, Shenzhen 518172, Guangdong, China

Published online: 16 April 2024

to pattern the graphene layer into periodic arrays forming a metasurface, such as strips [1, 12] and circles, to form a highly localized terahertz electromagnetic field. However, the carrier mobility of patterned graphene may be significantly reduced, and the precision of lithography can greatly affect the sensing performance [13, 14]. Coupling the evanescent wave with SPP in a metallic slip for optical modulators and sensing detectors has been widely reported and applied in the visible and infrared frequencies. Thus, similar plasmonic modulators and sensing devices can be constructed, as graphene can support SPP in the THz range. Pickwell-MacPherson et al. implemented a total internal reflection (TIR) arrangement to generate evanescent wave coupling with the graphene layer. They experimentally presented a THz light modulator with high modulation depth (> 90%) in broadband from 0.15 to 0.4 THz [15]. Similarly, using a higher refractive index (RI) prism, Hwang presented a design of an evanescent wave biosensor incorporating the surface plasmon resonance on a periodic graphene ribbons array [16]. Therefore, integrating a higher RI waveguide offers a practical strategy to improve vector matching, and exciting the plasmon [17, 18].

Similar to the TIR method, fiber functions as a high-caliber optical waveguide. Specifically, the photonic crystal fiber (PCF), with its adjustable and versatile structural characteristics, presents a fascinating approach to generating graphene plasmon. Consequently, the fusion of PCF with the graphene surface plasmon has attracted considerable interest and has been extensively studied in light modulation and sensors [19, 20]. Liu et al. experimentally constructed a half-meter-length graphene PCF modulator with strong light-matter interaction (~ 8 dB·cm^{-1} attenuation), broadband response (1150–1600 nm), and significant modulation depth (~ 20 dB·cm^{-1} at 1550 nm) [21]. With monolayer graphene located at the inner surface of the air hole near the core, Wang et al. designed a PCF sensor based on graphene plasmon. The frequency sensitivity is about 208.14 GHz/RIU, and the loss spectrum can be dynamically tuned by adjusting the Fermi energy within a sensitivity of 767.5 GHz/eV [22]. Here, RIU is short for refractive index unit, a property of the analyte measured with an Abel instrument [23]. In 2023, they theoretically designed a graphene plasmonic sensor based on D-shaped PCF, where the graphene layer is directly coated at the D-shaped surface plane. The average wavelength sensitivity is 305.5 μm/RIU while obtaining a maximum amplitude sensitivity of 30.85 RIU^{-1} [24]. Besides, Yao et al. proposed a tunable THz fiber modulator based on graphene-coated D-shaped fiber. The modulation depths of the two polarization states are 40.51% and 24.54% at 0.64 THz [25]. In these studies, the analyte is in contact with the graphene surface, thus modulating the graphene plasmon mode. The primary mechanism of these modulators and sensors involves the interaction between the core-guided light beam and the graphene surface plasmon. Moreover, the enormous structural flexibility of the PCF enables novel approaches to fill materials into its micro holes, which in turn can modulate the core-guided mode. This filling strategy has many applications, including mode-locked fiber lasers, surface plasmon generation, in-fiber Raman scattering, and light modulation devices [26, 27]. Consequently, if the detecting analyte is concurrently located in the core and sensing channel, new sensing and modulation phenomena may be achieved.

In this work, we theoretically demonstrate a graphene plasmonic resonance sensor based on liquid-core PCF, and the sensing performance is investigated by the finite element method (FEM). As the analyte is filled at the fiber core and graphene sensing channel, the analyte modulates both the GP and the core-guided mode. A negative RI sensitivity is observed for the first time in the THz plasmonic sensing setup. The detailed modulations of dispersion relations on analyte RI are studied to analyze the original mechanism. Additionally, the unique tunability property is also presented.

Theoretical Sensing Analysis

Structure Design and Simulation Model

The cross-sectional view of the proposed graphene plasmonic photonic crystal fiber is shown in Fig. 1a. It is an index-guiding PCF consisting of three layers of air holes arranged in a hexagonal way. A relatively big center hole with graphene coated in the inner wall carrying plasmon is used as the detecting channel filled with the analyte. Then, six liquid cores are formed by extending the corresponding air holes in the second layer with a diameter of 1.2 Λ and infilling the analyte with RI higher than the substrate [28]. Therefore, the index-guiding mechanism is guaranteed for each individual core, forming a multi-core graphene (MC-Gr) PCF sensor. With this arrangement, the light transmitted

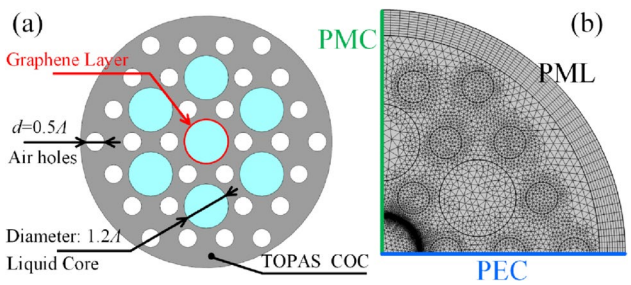

Fig. 1 **a** Cross-section of the designed multi-core PCF-based graphene plasmonic sensor. **b** FEM mesh and boundary conditions for the calculation. PML is short for a perfectly matched layer

in each core can excite the plasmon coupling on the graphene/analyte intersurface, and the signal-to-noise ratio (SNR) can be improved consequently. Note that the detecting analyte fills in both the multi-core and center channel marked with blue blocks. Therefore, the analyte can modulate both the graphene plasmon and core-guided mode. The red solid circle indicates the graphene nanosheet with extra-thin structure.

The center-to-center distance between air holes is called lattice constant with a value of $\Lambda = 600$ µm, and the air hole diameter is $d = 0.5\ \Lambda$. The radius of the center sensing channel is $0.6\ \Lambda$. For our investigation in a THz range, TOPAS cyclic olefin copolymer (COC) can be used to construct the fiber because of its near-zero material dispersion, low absorption, and high chemical resistivity [29]. Thus, the PCF's RI is assumed to be 1.5 RIU without considering the dispersion. The cladding hole is filled with air ($n_{\text{air}} = 1$). A full-vectorial FEM method is used to analyze its light propagation property, especially the mode coupling between the multicore and surface graphene plasmon. With the structure featuring a C_{6V} rotational symmetry, only a quarter of the PCF cross-section needs to be calculated. The perfect magnetic conductor (PMC) and perfect electric conductor (PEC) conditions are applied in the vertical and horizontal boundary to maintain the propagating mode [30]. The whole structure is discretized with triangular for calculation shown in Fig. 1b.

For the sheet structure of graphene with an extremely thin layer, a conductivity (σ_g) parameter is used to describe its property. According to the Kubo-equation, σ_g is the sum of two electron transitions called the intra-band term (σ_{intra}) and the inter-band term (σ_{inter}) [31, 32]. Because the low THz photon energy hardly induces the inter-band electron transition, only the intra-band electron transition (σ_{intra}) is considered:

$$\sigma_g \approx \sigma_{intra} = \frac{ie^2 k_B T}{\pi\hbar^2\left(\omega + \frac{i}{\tau}\right)}\left(\frac{E_f}{k_B T} + 2In\left(1 + \exp(-\frac{E_f}{k_B T})\right)\right) \tag{1}$$

Here, e, k_B, and $\hbar$ are universal constants, which symbolize the charge of an electron (1.6×10^{-19} C), the Boltzmann's constant (1.3806×10^{-23} $m^2kgs^{-2}K^{-1}$), and the reduced Planck constant [33]. E_f is the Fermi energy of graphene and has a trace of critical drive property by the bias voltage, which enables the sensor with dynamic tunability. As the graphene with low concentration doping ratio, $|E_f| >> K_B T$ and $\hbar\omega < 2|E_f|$ are considered. Thus, the contribution of intra-band can be simplified as follows [34]:

$$\sigma_g \approx \frac{e^2 E_f}{\pi\hbar^2}\frac{i}{\omega + i/\tau} \tag{2}$$

Here, τ is the relaxation time. Therefore, the graphene permittivity can be expressed as $\varepsilon_g = 1 + i\sigma_g/(\omega\varepsilon_0 t_g)$, where ε_0 is the vacuum permittivity. The graphene layer is ultra-thin with a t_g value of 0.34 nm.

Mode Analysis and Coupling Mechanism

The designed MC-PCF sensor is a superstructure and supports multiple super modes [30, 35]. Each mode has a specific electric field distribution with a corresponding effective refractive index, as shown in Fig. 2. As the real part of the effective RI decreases in a specific sequence, they are identified as super mode one, two, and three (SP1, SP2, and SP3 for short), respectively. For every individual mode, the distribution of the field exhibits a Gaussian profile without any splitting features, implying that these three modes are super modes rather than being of a higher mode [35]. In the case of the SP1 mode, the electric field orientations in adjacent cores are uniform (indicated by a light arrow), whereas for the SP2 and SP3, the field vectors exhibit variations. It is worth mentioning that the imaginary part of SP3 mode is much higher than the other two, suggesting that the SP3 exhibits significant loss properties when propagating over the same PCF length. On the other hand, the real components exhibit disparity as well. Consequently, these dispersion relationships have the potential to intersect with graphene plasmon modes within varied terahertz ranges, thereby inducing resonance coupling.

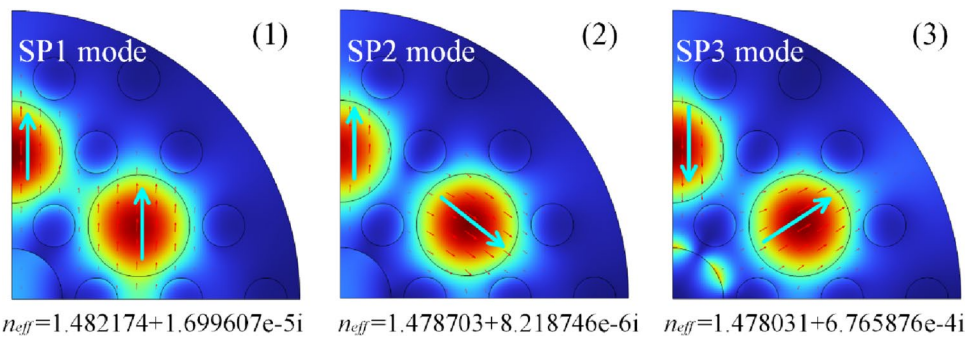

Fig. 2 Electric field distributions and corresponding effective RI (n_{eff}) for the super modes supported by the MC-PCF (analyte RI = 1.52, $f = 0.6$ THz, and $E_f = 0.6$ eV). The arrows represent the electric field direction

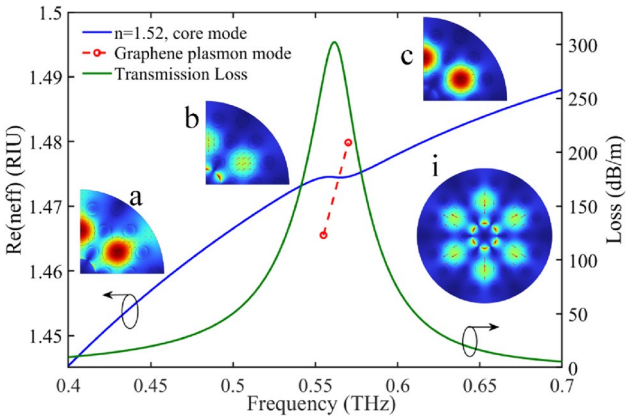

Fig. 3 Dispersion lines of core-guide and GP mode with the loss spectrum. The inserts a, b, and c are the optical field distribution at different ranges. Insert *i* is the electric field distribution of the whole cross-section at the resonance frequency

The spectral loss, which relies on the imaginary component of the effective index of the core mode, can be represented by the following relationship [36, 37]

$$a(dB/m) = 8.686 \cdot k_0 \cdot \mathrm{Im}\left(n_{eff}\right) \tag{3}$$

Here, k_0 is the wavelength number calculated as $k_0 = 2\pi/\lambda$. The dispersion relations of the core-guided SP3 and the GP mode, along with the loss spectra, are depicted in Fig. 3. An evident loss peak emerges at the intersection of the two dispersion lines, signifying the fulfillment of phase-matching conditions between the GP and SP3 mode. Consequently, a portion of the core-guided mode is transferred to the analyte/graphene intersurface, generating a graphene plasmon resonance. As a result, a loss peak manifests in the core transmission mode.

To clearly demonstrate the modulation mechanism, Fig. 3a–c provide a visual representation of the field distributions of the core mode across various frequency ranges. At lower frequencies, the core mode predominantly concentrates within the core area. As the frequency increases, the dispersion of GP mode rises faster than that of core-guided mode, and an intersection appears between these two. It indicates that a high matching degree is achieved. At the cross point, a greatly enhanced local field is generated at the analyte/graphene intersurface, as depicted in Fig. 3b. Simultaneously, the intensity of the core field is relatively diminished, indicating the transfer of core-guided mode to GP mode, resulting in a loss peak. Moreover, at higher frequencies, the electric field refocuses within the core due to phase mismatch. The utilization of the mirroring process reveals the full field distribution of the fiber cross-section at resonance, shown as insert (*i*). It suggests that the GP mode splits around the boundary. These field distribution characteristics indicate that the generated GP mode is a higher order. Furthermore, the core energy being partially transferred into the GP mode implies an incomplete coupling between graphene plasmon and core mode [35]. In addition, the mode coupling also causes the twist of the dispersion curve near the resonance [38, 39].

Sensing Performance

Negative Wavelength Sensing

The plasmonic sensor's detecting mechanism is ensured by the dependence of the graphene plasmonic mode on the analyte's RI. As the dispersion relations varying with analytes, here we focus on the RI dependence response. Figure 4a shows the corresponding loss spectra when the analyte varies from 1.51 to 1.58, taking the RIs of sensing liquid covering harmful drugs, oils, cholesterol, nicotine, and bacillus bacteria [40]. The spectra shift towards a higher frequency, and at the same time, the loss peak decreases dramatically. In contrast to the general trend where a higher RI corresponds to a longer wavelength, the designed PCF sensor exhibits a negative wavelength sensitivity. To understand this unique feature in detail, the dispersion relations of both the GP and SP3 modes are calculated and presented

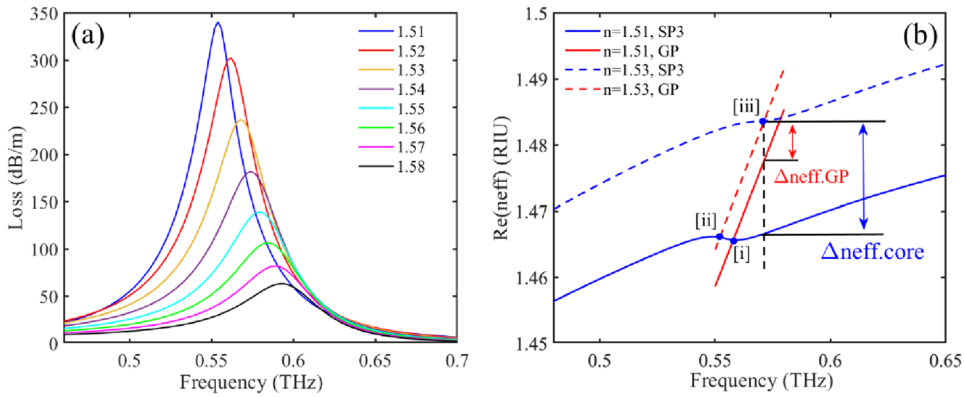

Fig. 4 **a** Resonance loss spectrum at different RIs. **b** Dispersion relations of both the core-guided SP3 mode and graphene plasmon at analyte RI of 1.51 (solid lines) and 1.53 (dotted lines)

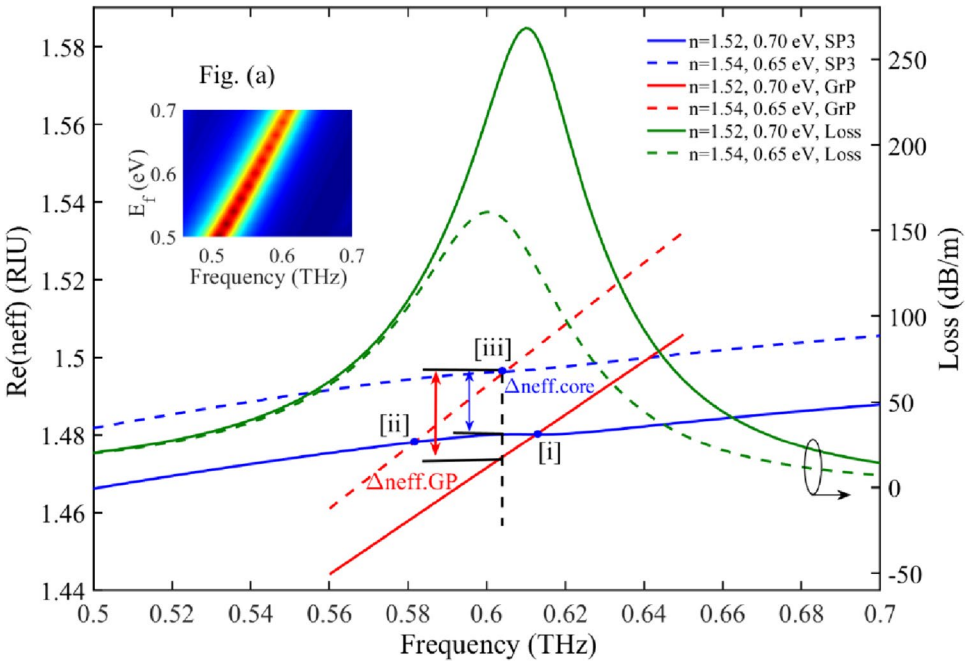

Fig. 5 Loss spectrum with dispersion lines of core-guided SP3 and GP mode at 1.52 RIU ($E_f = 0.7$ eV) and 1.54 RIU ($E_f = 0.65$ eV). Insert figure: loss spectrum at Fermi energies from 0.5 to 0.7 eV

in Fig. 4b. When the analyte RI increases from 1.51 to 1.53, both the GP and the SP3 mode experience modulation and move upwards. Assuming that the core mode (SP3) remains unaffected by varying analyte RI, the original phase matching point [i] moves to a lower frequency point [ii] due to the upward movement of the GP mode dispersion. However, because the core-guided dispersion also moves upwards with the increase in RI, the phase matching point [ii] undergoes a right shift and eventually moves to point [iii]. By defining the increment of an effective index as the modulation degree marked in Fig. 4b, the modulation degree of SP3 on the analyte (Δneff.core) is found to be 1.7075×10^{-2}, which is much higher than that of the graphene plasmonic mode ($\Delta\text{neff.GP} = 0.7081 \times 10^{-2}$). This results in the resonance moving towards a shorter wavelength (larger frequency) from point [i] to [iii]. Therefore, a larger upward movement corresponds to an enhanced modulation degree, meanwhile Δneff.GP and Δneff.core indicate the left and right frequency shift directions, respectively.

Positive Wavelength Sensitivity Based on Electric Tunability

Since the modulation relation of Δneff.core > Δneff. GP leads to a negative wavelength sensitivity, a counter situation can be obtained when Δneff.core < Δneff. GP. Fortunately, graphene's chemical potential (Fermi energy) can be easily controlled by adjusting its bias voltage, which allows us to increase Δneff.GP conveniently. Here is an example that demonstrates positive wavelength sensitivity. Figure 5 illustrates two loss spectra with dispersion lines, one at 1.52 RIU with $E_f = 0.7$ eV (solid lines) and the other at 1.54 RIU with $E_f = 0.65$ eV (dotted lines). A noticeable left shift is

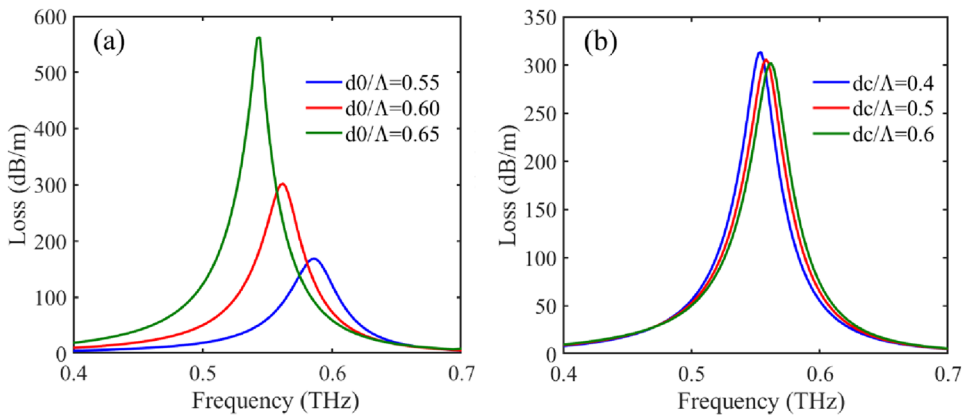

Fig. 6 Loss curves for PCF-based graphene plasmonic sensor with different parameters: center detecting channel d_0 (**a**), and cladding liquid core d_c (**b**). Simulation resolution: 0.002 THz

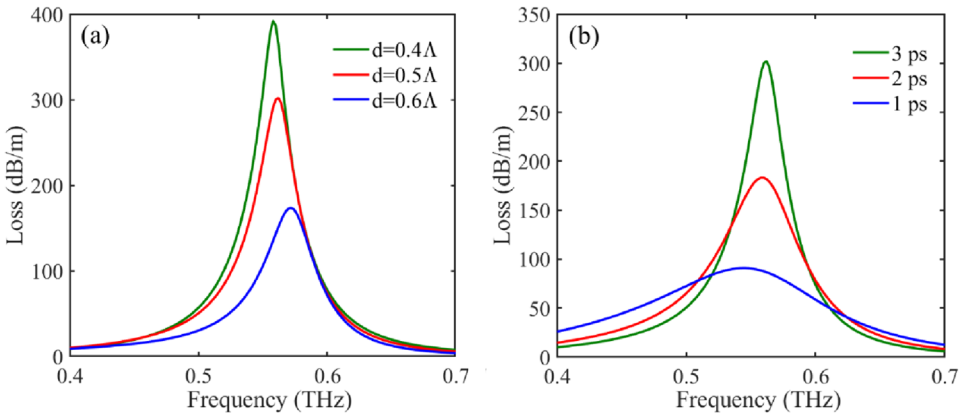

Fig. 7 The dependence of loss spectrum on cladding air hole diameter d (**a**) and carrier relaxation time τ (**b**)

observed in the resonance. This is mainly due to the higher modulation degree of the GP mode on the Fermi energy, resulting in Δneff.core < Δneff.GP. To be more specific, assuming that the core-guided mode is maintained, we only consider the GP mode's modulation by E_f. The original phase matching point [i] undergoes a left shift to the new position [ii] due to the decrease in E_f from 0.7 to 0.65 eV. Then, with an increase in RI, the intersection performs a relatively small right shift to point [iii]. In this case, Δneff.GP is 2.2302×10^{-2}, which is higher than Δneff.core $= 1.6171 \times 10^{-2}$. Additionally, the detailed tunability of the loss spectra on E_f is illustrated as the insert (a). The spectrum center can be efficiently adjusted from 0.510 to 0.612 THz, resulting in a tuning sensitivity of 510 GHz/eV. It is important to note that during the tuning, the peak intensity varies slightly. However, compared to RI = 1.52 ($E_f = 0.7$ eV), the loss spectrum of RI = 1.54 ($E_f = 0.65$ eV) is noticeably damped. Thus, this reduction is mainly caused by the RI modulation rather than the E_f. With an increase in RI, the core-cladding index contrast becomes enhanced. Then, the light is more restricted in the core area, leading to less energy transfer. As a result, the coupling degree weakens, and the loss spectrum decreases.

Geometry Dependence and Tunability of the Sensor

Geometry Dependence

Due to the flexible design of PCF's structure and to facilitate optimized sensing, we investigate the dependences of the loss spectrum on main structure parameters, i.e., central analyte diameter d_0, liquid-core diameter d_c, and cladding air hole (d), as illustrated in Figs. 6a, b and 7a, respectively. Among these parameters, the loss spectrum can be efficiently adjusted by d_0. With varying d_0 from 0.55 to 0.65 Λ, we observe a significant left shift (from 0.586 to 0.544 THz) and a substantial increase in the loss peak intensity (from 168.9 to 562.7 dB/m). This can be attributed to the fact that the GP mode dispersion moves upward with an increase in d_0. On the other hand, the core-guided SP3 mode remains unaffected by the changes in the sensing channel, resulting in a left shift of the dispersion intersection. For d_c in the range of 0.4–0.6 Λ, the loss spectrum exhibits a slight variation, allowing much flexibility in the sensor design.

Setting d as 0.4 Λ, 0.5 Λ, and 0.6 Λ, a right shift in resonance is observed, starting from 0.558 THz, then 0.562 THz, and finally reaching 0.572 THz. The intensity of the primary peak gradually decreases from 392.1 to 302.2 dB/m and then to 173.7 dB/m. This can be attributed to the reduction in the cladding effective index due to the increase in air hole diameter, which results in an enhancement of the core-cladding index contrast. Additionally, the dispersion relation of the core mode moves upwards. In contrast, the GP mode remains unaffected by

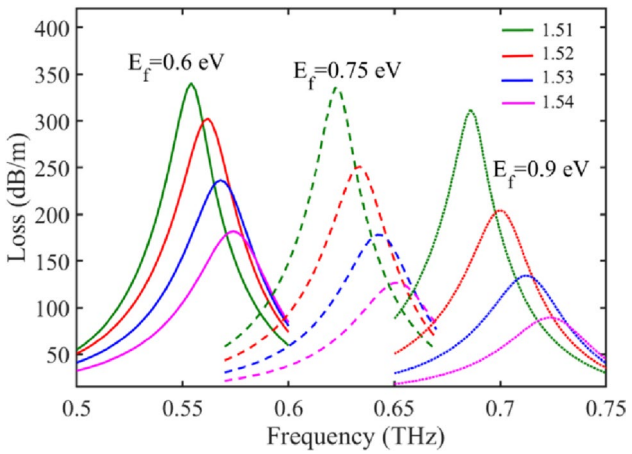

Fig. 8 Turnability of loss spectrum on Fermi energy from 0.6 to 0.9 eV, and corresponding RI sensing

Table 1 Comparison of the sensing performance at different E_f

E_f (eV)	0.6	0.75	0.9
Average sens. (THz/RIU)	0.6667	0.9667	1.2667
Intensity sens. ($\times 10^3$ dB/m/RIU)	5.2933	6.9567	7.4350
FWHM (@RI = 1.51 RIU)	~38 GHz	~36 GHz	~38 GHz

the variation in d, leading to the rightward movement of the phase matching point. Further calculation shows that increasing lattice weakens the resonance intensity without any frequency shift. Moreover, the carrier mobility, i.e., the relaxation time τ, serves as a critical parameter for evaluating the quality of graphene. As reported in unsuspended devices, the carrier mobility ranges from 2000 to 25,000 $cm^2/V/s$. For suspended systems, this value can reach up to 230000 $cm^2/V/s$ [41]. Figure 7b illustrates the impact of τ on the loss spectrum, where the resonance frequency remains relatively unchanged, but the peak intensity significantly decreases with decreasing τ. Simultaneously, the full width at half maximum (FWHM) broadens. In practical applications, a smaller FWHM is preferred to achieve a higher SNR, highlighting the importance of the graphene quality in sensing performance.

Tunability Based on the Fermi Energy (E_f)

The distinctive advantage of a graphene-based plasmonic sensor lies in its tunable ability, achieved through the adjustment of the Fermi energy (E_f). The specific details of this capability are elucidated in Fig. 8. This depiction reveals that the detection frequency, for a given RI range (1.51–1.54 RIU), can be artificially manipulated. As the E_f value increases within the range of 0.6 to 0.9 eV, the loss spectrum shifts from 0.554–0.574 THz to 0.686–0.724 THz, with a tuning sensitivity of 0.44 THz/eV. Furthermore, for each E_f value, the resonance spectrum behaves similarly, shifting towards the right and gradually decreasing with RI increase. The comprehensive sensing parameters can be concluded in Table 1. Both the frequency (changing from 0.6667 to 1.2667 THz/RIU) and intensity (ranging from 5.2933 to 7.4350×10^3 dB/m/RIU) sensitivities are enhanced at higher E_f values, while the FWHM remains relatively stable. Supposing the spectral resolution to be 0.01 THz (Terasys 4000, Rainbow Photonics), the detecting limitation may reach up to 0.0079 RIU [42]. It is worth noting that, for a specific RI value with increased E_f, the resonance intensity diminishes. Therefore, there is a need to carefully consider the trade-off between sensitivity and resonance depth in the detection process.

Different from conventional plasmonic sensors, the tunability of graphene plasmon can be flexibly controlled by manipulating its bias voltage. Thus, to detect specific analyte RIs, the measurement frequency can be shifted to a desired range, making full use of the limited bandwidth optical source or the narrowband spectrometer. As a result, a multi-series-channel system can be constructed by solely manipulating the E_f. In comparison to alternative methods for achieving an adjustable detection range, such as incorporating nano-porous silica coatings [43], introducing materials into a hollow fiber [44, 45], or reconfiguring the components of sensors [46, 47], the work presented here provides a convenient and feasible design that holds great potential for a wide range of applications. Moreover, with the tunability of the THz resonance spectrum via controlling its bias voltage, this sensing probe can also work as a switch for specific frequencies [48, 49]. Besides the tunability, the high sensitivity makes the designed sensor stand out from the comparison in Table 2.

For the fabrication process, the graphene layer can be obtained using the chemical vapor deposition (CVD) method. Then, with liquid etchants and solvents to delaminate graphene from its growth substrate, transfer the layer into the target channel in a liquid environment. Furthermore, the TOPAS COC can be fabricated using stack and draw-type techniques to ensure the smoothness of inner holes [54, 55].

Table 2 Performance comparison with relative work

Ref	Description of sensor	RI range	Frequency sensitivity (GHz/RIU)
[50]	Metamaterial absorber sensor	1.0–1.39	300 (average)
[22]	SPR sensor based on graphene PCF	1.0–1.5	208.14
[51]	Sensor based on graphene metamaterials	1.2–2.0	177.7
[24]	D-shaped PCF graphene SPR	1.0–1.4	220
[52]	Porous fiber/PVDF	1.0–1.01	749.5
[53]	D-shaped PCF/MoS_2	1.33–1.40	418.9
This	Liquid-core PCF-based graphene SPR	1.51–1.58	1266.7 (E_f = 0.9)

Conclusion

This paper investigates a graphene plasmonic sensor based on a core-filled PCF to demonstrate the dispersion analysis method and modulation properties. The analyte is filled at both the core and sensing material surface, resulting in simultaneous modulation of the core-guided mode and plasmon mode by the RI. The modulation degree of Δneff.core > Δneff.GP (or Δneff.core < Δneff.GP) produces a negative (or positive) wavelength sensitivity. Furthermore, the impact of the geometry on the sensor performance is analyzed. Utilizing graphene as a tunable plasmonic material, the detection frequency can be dynamically controlled within desired ranges. This enables the full utilization of a specific frequency range and presents a new flexible approach to constructing cascaded sensing channels. This innovative design and analysis method can be widely applied in other similar plasmonic sensing scenarios.

Author Contribution All authors contributed to the study conception and design. Material preparation, data collection, and analysis were performed by Syeda Aimen Abbasi, Ho-Pui Ho, Xuejin Li, and Wu Yuan. The first draft of the manuscript was written by Wei Luo and all authors commented on previous versions of the manuscript. All authors read and approved the final manuscript.

Funding This work was supported by the Research Grants Council (RGC) of Hong Kong SAR (ECS24211020, GRF14203821, GRF14216222), the Innovation and Technology Fund (ITF) of Hong Kong SAR (ITS/240/21), and the Science, Technology, and Innovation Commission (STIC) of Shenzhen Municipality (SGDX20220530111005039).

Data Availability Due to personal privacy and intellectual property protection, the datasets generated and analyzed during the current study are not publicly available but are available from the corresponding author on reasonable request.

Declarations

Competing Interests The authors declare no conflicts of interest.

References

1. Shen S et al (2022) Recent advances in the development of materials for terahertz metamaterial sensing. Adv Opt Mater 10(1):2101008
2. Degl'Innocenti, R., H. Lin, and M. Navarro-Cía, (2022) Recent progress in terahertz metamaterial modulators. Nanophotonics 11(8):1485–1514
3. Gezimati M, Singh G (2023) Terahertz cancer imaging and sensing: open research challenges and opportunities. Opt Quant Electron 55(8):727
4. Peng Z et al (2023) Broadband absorption and polarization conversion switchable terahertz metamaterial device based on vanadium dioxide. Opt Laser Technol 157:108723
5. Huang Y et al (2023) Reconfigurable THz metamaterial based on microelectromechanical cantilever switches with a dimpled tip. Opt Express 31(18):29744–29754
6. Li B, Lin Y-S (2023) Tunable terahertz metamaterial with polarization dependent and independent characteristics. Mater Res Bull 167:112444
7. Zeng Q et al (2024) Manipulating multiple plasmon modes by coupling fields for broadband filtering in terahertz metamaterials. Opt Laser Technol 168:109981
8. Fu X et al (2023) Graphene/MoS2− xOx/graphene photomemristor with tunable non-volatile responsivities for neuromorphic vision processing. Light: Sci Appl 12(1):39
9. Jain P et al (2023) Machine learning assisted hepta band THz metamaterial absorber for biomedical applications. Sci Rep 13(1):1792
10. Zhu J, Xiong J (2023) Tunable terahertz graphene metamaterial optical switches and sensors based on plasma-induced transparency. Measurement 220:113302
11. Luo W et al (2023) Electrically switchable and tunable infrared light modulator based on functional graphene metasurface. Nanophotonics 12(9):1797–1807
12. Li W, Zhao W, Cheng S et al (2023) Terahertz selective active electromagnetic absorption film based on single-layer graphene[J]. Surf Interfaces 40:103042
13. Yakimchuk E et al (2017) 2D printed graphene conductive layers with high carrier mobility. Curr Appl Phys 17(12):1655–1661
14. Wang B et al (2022) Ultra-broadband perfect terahertz absorber with periodic-conductivity graphene metasurface. Opt Laser Technol 154:108297
15. Liu X et al (2017) Graphene based terahertz light modulator in total internal reflection geometry. Adv Opt Mater 5(3):1600697
16. Hwang R-B (2021) A theoretical design of evanescent wave biosensors based on gate-controlled graphene surface plasmon resonance. Sci Rep 11(1):1999
17. Huang Y et al (2019) HR-Si prism coupled tightly confined spoof surface plasmon polaritons mode for terahertz sensing. Opt Express 27(23):34067–34078
18. Huang Y et al (2020) Terahertz plasmonic phase-jump manipulator for liquid sensing. Nanophotonics 9(9):3011–3021
19. Lou J et al (2019) Surface plasmon resonance photonic crystal fiber biosensor based on gold-graphene layers. Opt Fiber Technol 50:206–211
20. Ibrahimi KM, Kumar R, Pakhira W (2023) A graphene/Au/TiO2 coated dual-core PCF SPR biosensor with improved design and performance for early cancer cell detection of with high sensitivity. Optik 288:171186
21. Chen K et al (2019) Graphene photonic crystal fibre with strong and tunable light–matter interaction. Nat Photonics 13(11):754–759
22. Wang D et al (2022) Tunable surface plasmon resonance sensor based on graphene-coated photonic crystal fiber in terahertz. Appl Opt 61(22):6664–6670
23. Pal A et al (2022) A novel method for measurement of the refractive indices of transparent solid media using laser interferometry. The Physics Teacher 60(1):51–55
24. Wang D, Zhang Y, Tian J et al (2023) D-Shaped photonic crystal fiber with graphene coating for terahertz polarization filtering and sensing applications[J]. Opt Fiber Technol 79:103373

25. Wang S et al (2023) Graphene-coated D-shaped terahertz fiber modulator. Frontiers in Physics 11:1202839
26. Alam MK et al (2023) Design of highly sensitive biosensors using hollow-core microstructured fibers for plasma sensing in aids with human metabolism. Opt Quant Electron 55(2):188
27. Vyas AK, Gangwar RK, Kumar S (2022) Elliptical air hole PCF-based low-cost sensor for refractive index and temperature detection: Design and analysis. Opt Fiber Technol 73:103060
28. Khanikar T, Singh VK (2023) A highly sensitive liquid–filled microstructured fiber spr sensor for refractive index and temperature measurement. Plasmonics 18(1):95–104
29. Bao H et al (2012) Fabrication and characterization of porous-core honeycomb bandgap THz fibers. Opt Express 20(28): 29507–29517
30. Shuai B, Xia L, Liu D (2012) Coexistence of positive and negative refractive index sensitivity in the liquid-core photonic crystal fiber based plasmonic sensor. Opt Express 20(23):25858–25866
31. Vakil A, Engheta N (2011) Transformation optics using graphene. Science 332(6035):1291–1294
32. Bonaccorso F et al (2010) Graphene photonics and optoelectronics. Nat Photonics 4(9):611–622
33. Xiao S et al (2018) Active modulation of electromagnetically induced transparency analogue in terahertz hybrid metal-graphene metamaterials. Carbon 126:271–278
34. Li C, Yang R (2022) Generating different polarized multiple Fano resonances for highly sensitive sensing using hybrid graphene–dielectric metasurfaces. Opt Lett 47(22):5833–5836
35. Shuai B et al (2012) A multi-core holey fiber based plasmonic sensor with large detection range and high linearity. Opt Express 20(6):5974–5986
36. Luo W et al (2021) Surface plasmon resonance sensor based on side-polished D-shaped photonic crystal fiber with split cladding air holes. IEEE Trans Instrum Meas 70:1–11
37. Luo W et al (2021) Temperature effects on surface plasmon resonance sensor based on side-polished D-shaped photonic crystal fiber. Measurement 181:109504
38. Luo W et al (2023) Analysis of the D-shaped PCF-based SPR sensor using Resonance Electron Relaxation and Fourier domain method. Opt Lasers Eng 166:107588
39. Wang Y et al (2022) High-sensitivity refractive index sensing and broadband tunable polarization filtering characteristics of D-shaped micro-structured fiber with single-layer air-holes and gold film based on SPR. J Lightwave Technol 40(3):863–871
40. Kumar A, Verma P, Jindal P (2021) Refractive index sensor for sensing high refractive index bioliquids at the THz frequency. JOSA B 38(12):F81–F89
41. Khan MAK, Shaem TA, Alim MA (2020) Graphene patch antennas with different substrate shapes and materials. Optik 202:163700
42. Hoque AMT et al (2022) Dual polarized surface plasmon resonance refractive index sensor via decentering propagation-controlled core sensor. Optics Continuum 1(7):1474–1488
43. Chen Y et al (2016) Refractive index detection range adjustable liquid-core fiber optic sensor based on surface plasmon resonance and a nano-porous silica coating. J Phys D Appl Phys 49(35):355102
44. Zhang X et al (2022) Surface plasmon resonance temperature sensor with tunable detection range based on a silver-coated multi-hole optical fiber. Opt Express 30(26):48091–48102
45. Zhang X, Ding J, Zhu XS et al (2023) Hollow-core fiber sensor based on the long-range Tamm plasmon polariton with enhanced figure of merit[J]. Results Phys 53:107035
46. Xu J, Chen Y (2018) Surface plasmon resonance sensing with adjustable sensitivity based on a flexible liquid core coupling unit. Talanta 184:468–474
47. Mumtaz F et al (2023) Computational study: windmill-shaped multi-channel SPR sensor for simultaneous detection of multi-analyte. Measurement 207:112386
48. Dehghan M et al (2020) Bistable terahertz switch designed by integration of a graphene plasmonic crystal into Fabry-Perot resonator. IEEE J Sel Top Quantum Electron 27(1):1–6
49. Dehghan M et al (2023) Bidirectional terahertz plasmonic switch based on periodically structured graphene. JOSA B 40(7):1773–1778
50. Saadeldin AS et al (2019) Highly sensitive terahertz metamaterial sensor. IEEE Sens J 19(18):7993–7999
51. He X et al (2016) Tunable ultrasensitive terahertz sensor based on complementary graphene metamaterials. RSC Adv 6(57):52212–52218
52. Hassani A, Skorobogatiy M (2008) Surface plasmon resonance-like integrated sensor at terahertz frequencies for gaseous analytes. Opt Express 16(25):20206–20214
53. Liu S et al (2021) D-shaped surface plasmon resonance biosensor based on MoS2 in terahertz band. Opt Fiber Technol 66:102631
54. Jena R et al (2011) Large-strain thermo-mechanical behavior of cyclic olefin copolymers: application to hot embossing and thermal bonding for the fabrication of microfluidic devices. Sens Actuators, B Chem 155(1):93–105
55. Mavrona E et al (2021) Optimized 3D printing of THz waveguides with cyclic olefin copolymer. Opt Mater Express 11(8):2495–2504